Sensitivity Analysis of a Moist 1D Eulerian Cloud Model Using Automatic Differentiation

SEON KI PARK AND KELVIN K. DROEGEMEIER

Center for Analysis and Prediction of Storms and School of Meteorology, University of Oklahoma, Norman, Oklahoma

(Manuscript received 30 July 1997, in final form 14 July 1998)

ABSTRACT

An automatic differentiation tool (ADIFOR) is applied to a warm-rain, time-dependent 1D cloud model to study the influence of input parameter variability, including that associated with the initial state as well as physical and computational parameters, on the dynamical evolution of a deep convective storm.

Storm dynamics are found to be controlled principally by changes in model initial states below 2 km; once perturbed, each grid variable in the model plays its own unique role in determining the dynamical evolution of the storm. Among all model-dependent variables, the low-level temperature field has the greatest impact on precipitation, followed by the water vapor field. Mass field perturbations inserted at upper levels induce prominent oscillations in the wind field, whereas a comparable wind perturbation has a negligible effect on the thermodynamic field. However, the wind field does influence the precipitation in a more complex way than does the thermodynamic field, principally via changes in time evolution.

The simulated storm responds to variations in three physical parameters (the autoconversion/accretion rate, cloud radius, and lateral eddy exchange coefficient) largely as expected, with the relative importance of each, quantified via a relative sensitivity analysis, being a strong function of the particular stage in the storm's life cycle.

1. Introduction

The practical utility of numerical weather prediction models depends upon a number of important factors including the governing equations and their numerical representation, the sophistication and appropriateness of physical parameterizations, the quality of input data, and strategies used to fit the model to the data (i.e., data assimilation). Given this complexity and the nonlinear behavior of the flows represented by such models, it is important to understand how the model solution responds to changes in physical and computational parameters as well as the initial state. *Sensitivity analysis* is a general term for strategies that seek to obtain such an understanding, and broadly speaking, the problem may be approached using either a statistical or deterministic approach (e.g., Worley et al. 1987; Cacuci 1988).

In the *statistical* approach, one computes a relatively limited number of *exact* sensitivities by repeated execution of a full nonlinear model (NLM) for which appropriate variations are made to parameters of interest relative to a control case (e.g., Seigneur et al. 1981). This information is then used to assess sensitivity, sometimes over ranges beyond those for which information was actually generated. Such methods require tremendous amounts of computer time yet are able to deal only with a small subset of the full parameter space. In that regard, their practical usefulness is quite limited.

In the *deterministic* approach, one develops a set of differential *sensitivity equations* that are used to *approximate* the changes in model outputs as a function of changes in inputs. *Sensitivity coefficients* (i.e., the derivative or, in general, the gradient of the model solution vector with respect to inputs) are then computed by solving the differential sensitivity equations using a nonlinear solution as a basic state (e.g., Errico and Vukicevic 1992). In this regard the sensitivity is *complete* (i.e., valid for all ranges), but represents the true sensitivity only insofar as the linearity assumption is valid.

There exist three principal methods within the deterministic framework for computing sensitivity coefficients for either linear (first order) or nonlinear (high order) analysis: the Green's function method (GFM) (Hwang et al. 1978), the direct method (Dickinson and Gelinas 1976), and the adjoint method (Errico and Vukicevic 1992).

Ignoring the GFM, which has been applied primarily to chemical kinetics problems, we note that the direct method can be divided into two subsets: the direct *dif-*

Corresponding author address: Dr. Seon Ki Park, Cooperative Institute for Mesoscale Meteorological Studies, University of Oklahoma, Room 1110, Sarkeys Energy Center, 100 East Boyd, Norman, OK 73019.
E-mail: skpark@cmrp.ou.edu

ferential method (DDM) (Dickinson and Gelinas 1976) and the direct *perturbation* method (DPM) (Park et al. 1994; Wang et al. 1995). Through the direct differentiation of the NLM equations with respect to a specific parameter, the DDM involves deriving differential equations that govern the evolution of the sensitivity coefficients. In contrast, the DPM involves a tangent linear model (TLM) that describes the evolution of perturbation fields relative to a time-dependent base state (usually the solution of a nonlinear model). Both equation sets allow one to compute the sensitivities of all model outputs with respect to a particular input through forward time integration. Because the sensitivity equations are solved for each input, this method can be expensive when the number of inputs is large.

The adjoint method involves computing sensitivity coefficients of a specific output functional (i.e., dependent variables or quantities derived therefrom) with respect to all input parameters through a backward integration in time of the adjoint model [a transpose of the TLM; e.g., Errico and Vukicevic (1992)]. When applied to a model with more inputs than outputs, this method yields significant computational savings relative to the direct methods described above.

In the present study, we apply a combination of the above methods to *evaluate the sensitivity of numerically simulated convective storm evolution to initial conditions and selected control parameters using a one-dimensional moist cloud model.* Although simple in many respects, such models have proven extremely valuable for investigating the microphysical and dynamical characteristics of cumulus clouds (e.g., Wisner et al. 1972; Ferrier and Houze 1989; Weinstein 1970; Wang 1983; Ogura and Takahashi 1971; Curic and Janc 1989, 1993).

To facilitate our evaluation of sensitivity, we apply an automatic differentiation tool (ADIFOR; Bischof et al. 1992) to the 1D model. As described in section 2, ADIFOR provides a straightforward and computationally efficient method for obtaining sensitivity information. Because this work represents the first attempt to study convective storm sensitivity using automatic differentiation techniques, we chose the 1D cloud model framework for its completeness in basic physical processes as well as its computational simplicity. Using the results reported herein as a starting point, Park (1996) extended the sensitivity analysis to a fully 3D cloud model, and the results from that study will be reported in an upcoming paper.

We begin in section 2 by describing the methodology and introducing ADIFOR. Section 3 presents the control simulation, and in section 4, the derivative code of the 1D cloud model is applied to evaluate sensitivities of model outputs with respect to selected inputs. Section 5 provides a summary, conclusions, and recommendations for future research.

2. Computation of sensitivity coefficients

In order to generate the desired sensitivity information for our 1D model without creating its adjoint or resorting to similarly complicated techniques (see section 1), we apply here an automatic differentiation tool known as ADIFOR (Automatic Differentiation of Fortran: Bischof et al. 1992). ADIFOR effectively applies the chain rule repeatedly to elementary model operations to create a Fortran code that may be used to compute derivatives. It has been applied to a convective cloud model (Park et al. 1994; Park and Droegemeier 1995), a mesoscale model (Bischof et al. 1996), and most recently an air pollution model (Carmichael et al. 1997).

Of particular advantage in the present study is that, for a single model run, one can compute efficiently the derivatives of all model output variables and related diagnostic parameters (dependent variables, hereafter DVs) with respect to all input parameters (independent variables, hereafter IVs) including initial and boundary conditions as well as physical and computational constants. ADIFOR provides additional flexibility to compute other types of derivatives, as described in Park (1996). The reader is referred to Bischof et al. (1992) and Park (1996) for a complete description of ADIFOR.

We verified the ADIFOR-generated sensitivity coefficients against those produced by a hand-coded tangent linear version of our nonlinear cloud model. The results agreed to 12 digits of accuracy (Park 1996). Nonlinear perturbation experiments (e.g., Park and Droegemeier 1997, henceforth PD97) were likewise performed to validate both the tangent linear model and sensitivity coefficients, and similar agreement was obtained.

It is important to note that the code generated by ADIFOR for computing derivatives assumes that the cloud model solutions are continuous. This is a reasonable assumption for very small perturbations (e.g., PD97); however, for the magnitude of some perturbations used in the present study, the first-order tangent linear assumption may be violated (PD97), rendering the sensitivity information invalid. Such instances will be identified in the discussion that follows.

3. Numerical model and control simulation

We employ for the present study the 1D cloud model used in PD97. The environmental sounding and computational scheme used for our control simulation are the same as those of case A3 in PD97. That is, the ambient temperature, the surface value of which is 25°C, decreases at a rate of 8.6°C km^{-1} up to 1 km and then falls off at the moist-adiabatic lapse rate to the top of the domain (10 km). The relative humidity, which is 94.5% at the surface, increases linearly to 99.5% at 1 km and then decreases at a rate of 5% km^{-1} thereafter. The surface pressure is 1000 mb.

Convective motion is initiated by introducing, at the initial time only, a small updraft of parabolic shape from the ground to 1.75 km. The maximum value is 1 m s^{-1} at $z = 1$ km (see PD97 for additional details). The domain is divided into 41 vertical levels with a grid

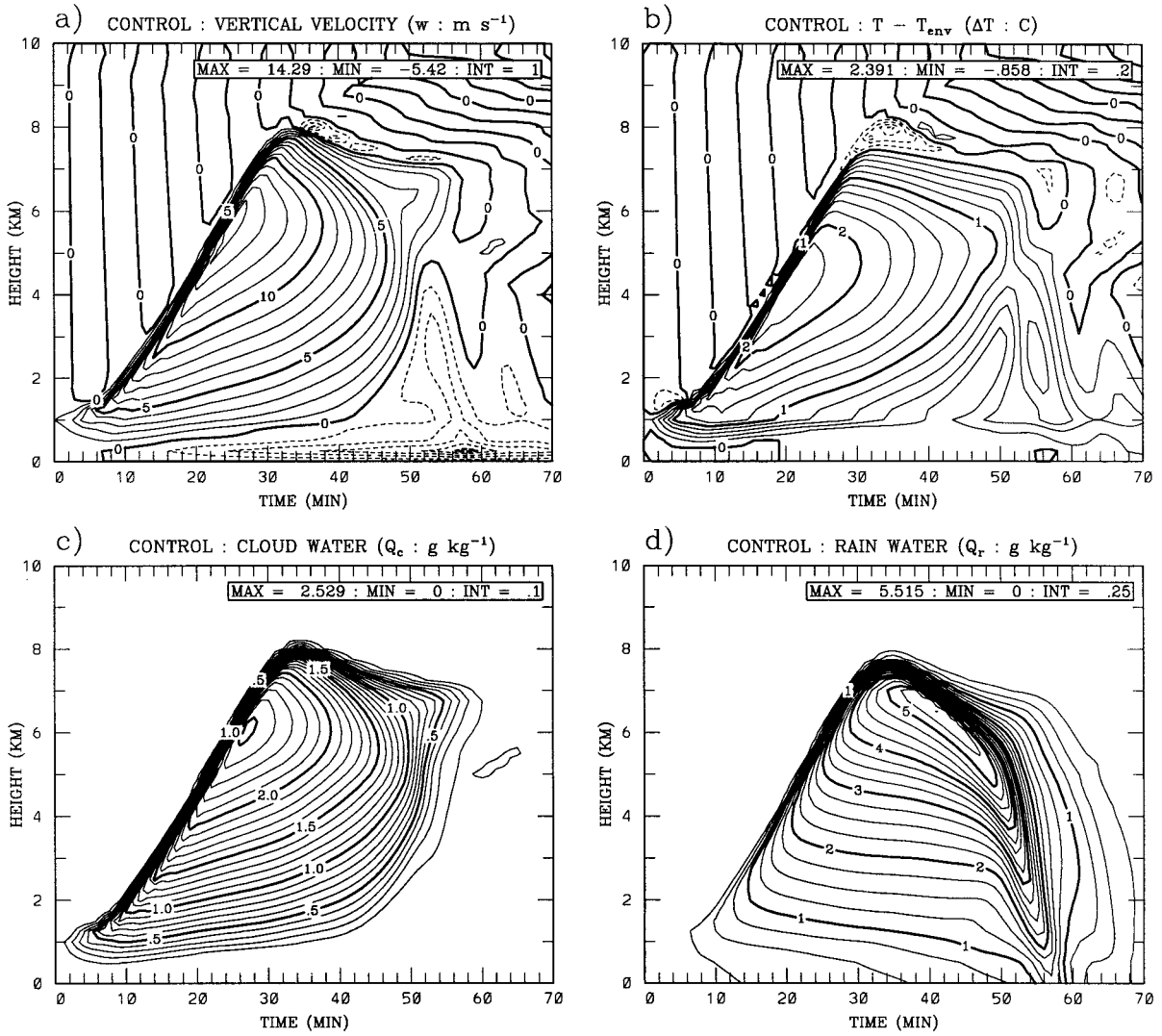

FIG. 1. Control forecast for (a) vertical velocity (w, in m s^{-1}), (b) temperature difference (ΔT, in °C), (c) cloud water mixing ratio (Q_c, in g kg^{-1}), and (d) rainwater mixing ratio (Q_r, in g kg^{-1}). The maximum (MAX) and minimum (MIN) are shown on each plot, along with the contour interval (INT).

interval of 250 m. A time step of 1 s is used, and all other model features are as described in PD97. As noted below (see also PD97), the model neglects the vertical pressure gradient force.

Figure 1 shows the vertical velocity (w), temperature deviation between the cloud and environment (ΔT; i.e., $T - T_{\text{env}}$), and the mixing ratios of cloud water (Q_c) and rainwater (Q_r) for the control experiment. The updraft grows rapidly due to positive thermal buoyancy induced by condensational heating, with local maxima observed near cloud top (Fig. 1a). The maximum updraft of 14.3 m s^{-1} occurs at $t = 26$ min at $z = 5.75$ km; thereafter, the height of the maximum updraft slowly drops with time. At ~7 min, a downdraft develops first at lower levels and then spreads to higher altitudes to occupy a major portion of the cloud at ~50 min. The maximum downdraft of −5.4 m s^{-1} is observed near the ground at 58 min. The maximum temperature excess of 2.4°C occurs earlier (~22 min) and at lower levels (~4.5 km) than the maximum updraft. Following the standard three-stage life cycle of an ''airmass'' storm, we denote the *growing stage* (0–7 min) when the cloud is primarily updraft, the *mature stage* (7–50 min) when both updraft and downdraft are present, and the *decaying stage* (50–70 min) when downdrafts dominate.

Throughout the life of the cloud, downdrafts at low levels (≲1 km) are driven mostly by negative thermal buoyancy resulting from the evaporative cooling of cloud and rain water. Downdrafts at midlevels (from 1 to 5 km) during the decaying stage are forced principally by liquid water drag. After the cloud is fully developed, strong downdrafts are also observed near cloud top, mostly as a result of the cloud overshooting the equilibrium level.

It is interesting that a local maximum in ΔT is collocated with the downdraft during the decaying stage ($\sim$2.5 km around 55 min). The air in this region is unsaturated after the cloud decays; that is, air parcels, which subside as a result of liquid water drag, warm adiabatically in the region of subsaturation. This results in a temperature excess even though evaporative cooling is also present. As the parcels descend farther, the temperature excess decreases because the downward forcing by liquid water drag weakens and evaporative cooling strengthens. In addition, the greater environmental lapse rate below 1 km, still less than dry adiabatic, reduces the temperature excess further (Srivastava 1985).

The water vapor perturbation (ΔQ_v; i.e., $Q_v - Q_{v\text{env}}$) is a maximum (2.38 g kg^{-1}) at 15 min and 2.5 km (not shown), which is both earlier and at a lower level than for the maximum in ΔT. As the downdraft proceeds, a water vapor deficit is observed below cloud base after 16 min. The pattern of cloud water development follows that of the updraft (Fig. 1c), with a maximum in Q_c of 2.5 g kg^{-1} at $z = 6$ km at $t = 26$ min. The highest cloud water contents are observed near cloud top until 26 min. The maximum height of cloud top is 8.25 km at 34 min, and thereafter slowly decreases. The cloud dissipates as the downdraft develops, and the cloud at lower levels decays earlier than that at higher levels.

The axis of maximum Q_r (AMQ_r) appears just below cloud top until the highest rainwater content occurs at $z = 6.5$ km around $t = 40$ min (Fig. 1d). After that, the AMQ_r tilts downward with time, implying precipitation loading. It is apparent that cloud and rain species are advected upward near cloud top as the updraft develops, accumulating there while the updraft intensifies. As Q_r increases via conversion/coalesence and the terminal velocity overcomes the updraft, the downdraft is enhanced by liquid water drag. Rain sedimentation is also observed during the early mature stage when the updraft is not strong enough to overcome the terminal velocity.

We observe gravitational oscillations in w and ΔT (and in ΔQ_v, not shown) with a period of $\sim$10 min above cloud top (see Figs. 1a and 1b). They are initiated by adiabatic cooling above the rising cloud as the updraft intrudes into the unsaturated stable layer above. These oscillations are associated with gravity waves, whose period is consistent with $2\pi/N$ where N is the buoyancy frequency (Holton 1992). This behavior is often exaggerated in simple cloud models (e.g., Wisner et al. 1972; Soong and Ogura 1973; Ogura and Takahashi 1973) and in the absence of wind shear. Exceptionally strong gradients in all fields are observed near cloud top due to known model deficiencies, particularly the neglect of the vertical pressure gradient force and vertical mixing (Ogura and Takahashi 1973; see also PD97).

The dynamic evolution of storms simulated by this model is very sensitive to the cloud-to-rain conversion process, which in our model (following Ogura and Takahashi 1971) is a combined, very simple representation of the traditional autoconversion and accretion effects (see appendix of PD97). The autoconversion/accretion rate (C_0) is the controlling factor. We use $C_0 = 0.005$ s^{-1} in the control simulation, which corresponds to a conversion time of $\sim$3.3 min. When C_0 is sufficiently large (i.e., the conversion time is short), rain is produced rapidly and the associated drag leads to an earlier decay of the cloud (see below). As indicated in PD97, the cloud shows a change in regime from steady state to nonsteady behavior as C_0 increases above $\sim 4.096 \times 10^{-3}$ s^{-1}.

As a basis for the linear sensitivity results to follow, we examine briefly the nonlinear change in storm characteristics induced by prescribed changes in C_0. Figure 2 shows time series of domain-wide extrema in vertical velocity ($w_{\max}$ and $w_{\min}$), total liquid water content (TLWC), surface rainfall rate (SRR), and accumulated rainfall (ARF) for simulations using $C_0 = 0.005$ s^{-1} (control case) and $C_0 = 0.01$ s^{-1} (perturbation case). Here, the TLWC is obtained by summing up the liquid water contents (LWC) at all vertical levels; that is,

$$\text{TLWC} = \sum_k \text{LWC}(k),$$

for LWC (k) defined at a level k as

$$\text{LWC}(k) = 10^6 \times \rho(k)[Q_c(k) + Q_r(k)],$$

where ρ is air density (in g cm^{-3}) and Q_c and Q_r are mixing ratios of cloud water and rain water, respectively (in g g^{-1}). The units of LWC and TLWC are grams per cubic meter.

The vertical velocity extrema are reasonably similar until approximately 10 min, after which the updraft in the perturbation case decreases its rate of growth, levels off, and then begins to decay very rapidly in response to the rapid rate of autoconversion/coalesence relative to the control run. The downdraft of the perturbation case is also slightly stronger, consistent with this effect. The TLWC of the perturbation case begins to decrease much earlier than the control case because rain is produced more quickly and falls out of the cloud at a faster rate. Thus, the lifetime of the storm is shortened considerably with only a factor of 2 change in C_0. This overall behavior is clearly evident in Figs. 2c and 2d, which show that the more rapid autoconversion/coalesence rate in the perturbation case results in substantially higher surface rain rates and accumulated precipitation.

4. Sensitivity results

a. Sensitivity to physical parameters

We now explore the changes in cloud behavior brought about by changes in three physical parameters: the cloud-to-rain autoconversion/accretion rate (C_0), the lateral eddy exchange coefficient (α), and the radius of the cloud (R; see the appendix of PD97 for a complete

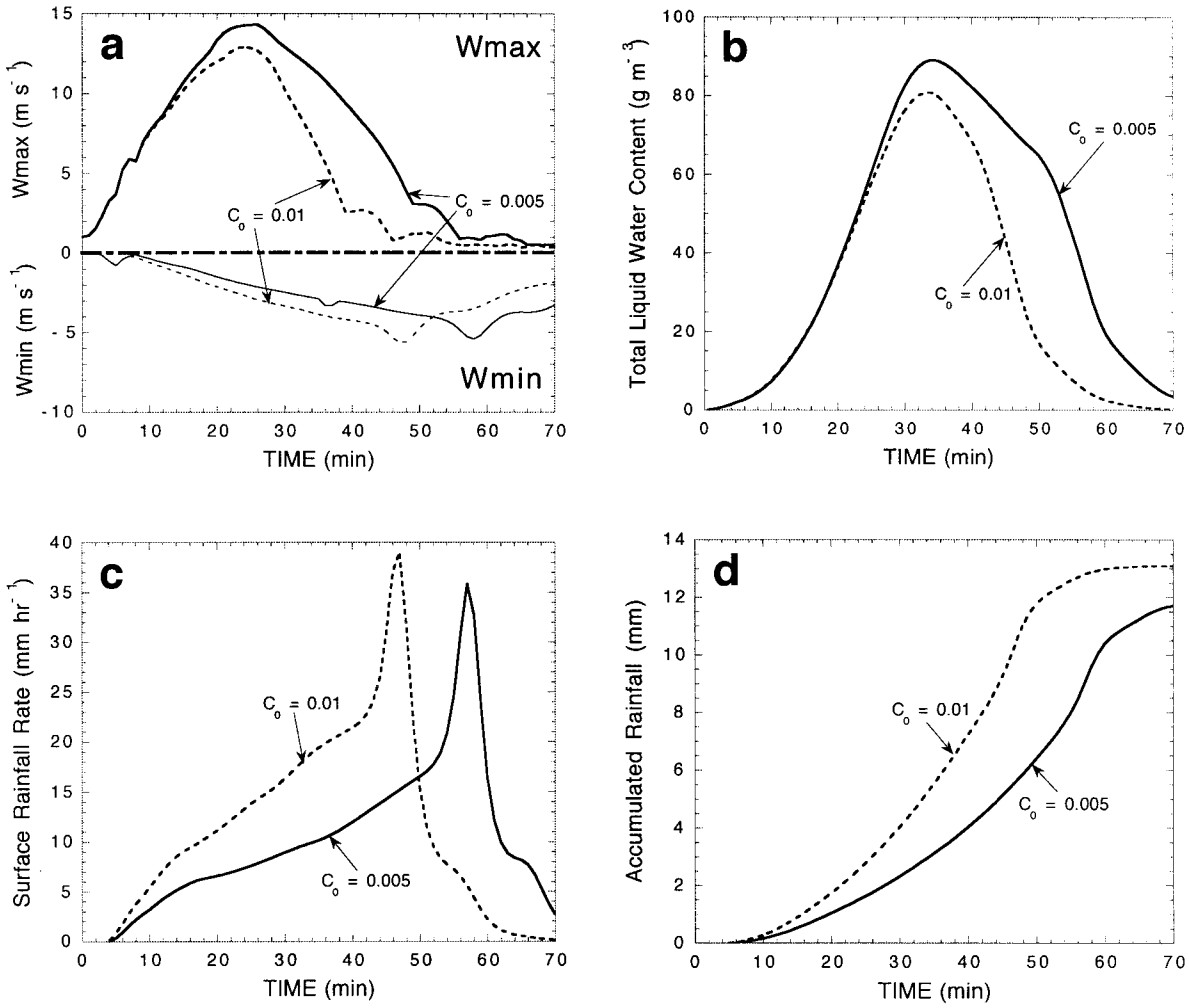

FIG. 2. Characteristics of simulated storm for $C_0 = 0.005\ s^{-1}$ (solid line) and $C_0 = 0.01\ s^{-1}$ (dashed line). Evolution of (a) w_{max} (thick lines) and w_{min} (thin lines) (in m s^{-1}), (b) TLWC (in g m^{-3}), (c) SRR (in mm h^{-1}), and (d) ARF (in mm).

description of these parameters). The values of these parameters in the control run are 0.005 s^{-1}, 0.2, and 3 km, respectively.

Figure 3 shows the sensitivity coefficients (i.e., derivatives) of TLWC, SRR, and ARF [indicated by $J(t)$ in the figure, i.e., the dependent variables or forecast aspects] with respect to C_0, α, and R (the independent variables). Because each coefficient has a different physical dimension, their relative importance will be addressed later through the use of relative sensitivity coefficients. Focusing first on C_0 (Fig. 3a), the SRR sensitivity is positive [i.e., an increase (decrease) in SRR results from an increase (decrease) in C_0] and increases in value until about 56 min, at which time it abruptly decreases, reaching a negative peak just before 60 min. It increases thereafter, though remaining negative. During this same time, the TLWC sensitivity, which is always negative in this experiment, reaches its peak value at the time the SRR sensitivity shifts from positive to negative. The ARF sensitivity shows little fluctuation during this time interval, albeit for a peak positive value at the zero crossing of the SRR curve (simultaneous with the peak downdraft intensity at 58 min).

The extent to which these three quantities are related is apparent when one recognizes that the SRR and ARF increase at the expense of the TLWC in the region of strong downdraft. The abrupt sign change in SRR within a very short time (3 min from the negative peak to the positive peak) is related to the leftward movement of the maximum SRR along the time axis. That is, as C_0 increases (i.e., as the conversion time becomes shorter), rain is produced more rapidly at upper levels, thereby increasing the downward rain flux and the surface rain rate. Consequently, the cloud decays earlier due to the combined effects of liquid water drag and evaporation. The observation that significant sensitivities occur only after ~40–50 min is a result of the fact that variations in C_0 have an appreciable impact only after significant rain and cloud water have developed.

The sensitivity of TLWC with respect to α (Fig. 3b)

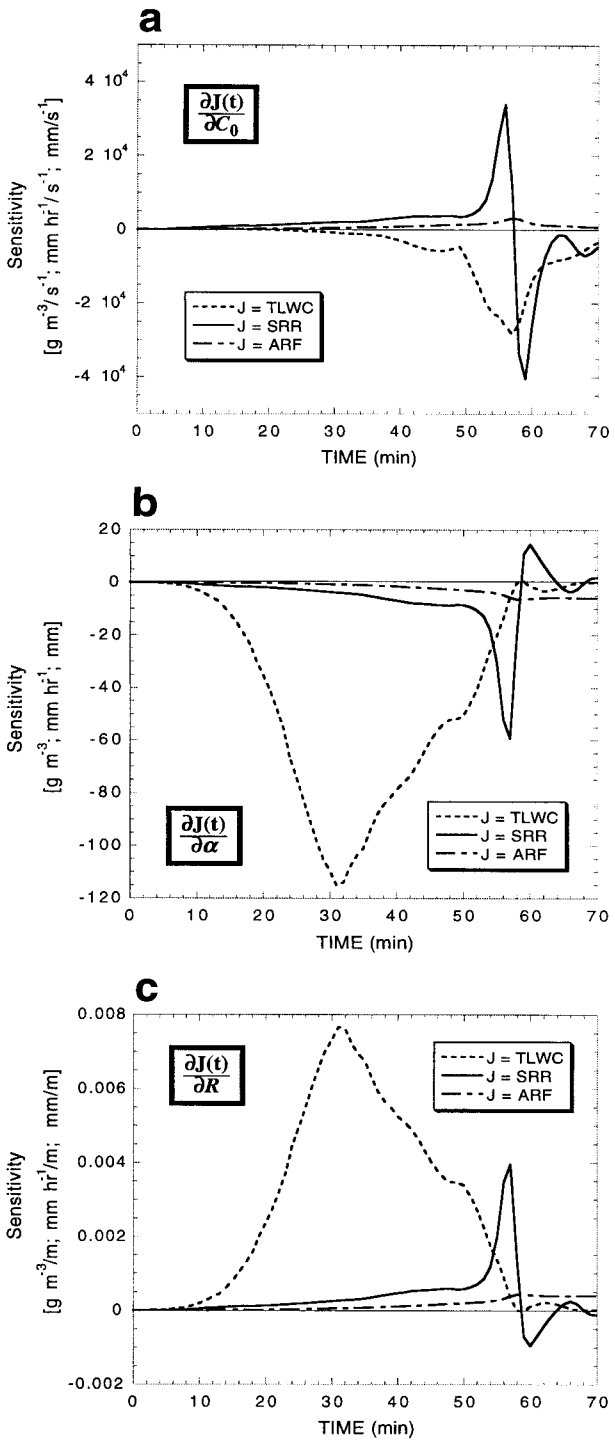

FIG. 3. Sensitivities of TLWC, SRR, and ARF with respect to (a) C_0, (b) α, and (c) R. Units are described in each figure in the order of TLWC, SRR, and ARF.

is negative throughout the simulation and is marked by a monotonic decrease during the mature stage; the minimum is reached at 31 min (Fig. 3b). The sign of this sensitivity is explained by noting that the mixing of dry air through the lateral boundary of the cloud leads to less condensation and thus a smaller TLWC. The greater the entrainment coefficient, the greater is the *reduction* in TLWC. As the storm begins to rain out and decay, the sensitivity begins to increase and becomes negligible around 58 min.

The SRR sensitivity to α is negative and decreases slowly, reaching a peak at 57 min. It then increases rapidly, becoming positive at 58 min and reaching a maximum at 60 min. In contrast to the C_0 sensitivity results, this implies a rightward movement of the maximum SRR along the time axis and thus an extension of the storm's lifetime. That is, as α increases, the storm develops more slowly but lives longer. In this case, it is apparent that the ARF sensitivity is negative and decreases with time, as shown in Fig. 3b.

Changes in storm features due to variations in cloud radius R (Fig. 3c) behave in a manner opposite to those induced by changes in α (cf. Fig. 3b). Increasing the radius of the cloud reduces the effect of dry air entrainment near the core of the updraft. In addition, the TLWC is closely related to updraft intensity (cf. Figs. 2a and 2b); therefore, changes in TLWC induced by variations in α and R are the largest during the mature stage, that is, when the updraft is the strongest. In contrast, the SRR and ARF are more closely tied to the behavior of the downdraft, which is a maximum during the decaying stage.

Because the sensitivities in Fig. 3 have different physical dimensions, it is difficult to quantify their relative importance. To overcome this limitation, one can compute *relative (or normalized) sensitivity coefficients* (RSC; Sykes et al. 1985), which are defined simply as the sensitivity coefficient divided by its control run counterpart. Thus, while the sensitivity coefficients shown in Fig. 3 depict the change in a DV with respect to a unit change in an IV, the RSC represents the percentage change in a DV with respect to a 1% change in the IV.

Table 1 shows the RSCs at 35 min for the same DVs and IVs as in Fig. 3. The TLWC is found to be more strongly influenced by parameters related to the lateral eddy exchange (α and R) than the autoconversion/accretion factor (C_0); changes in rainfall-related DVs (SRR and ARF) show the opposite behavior. This makes sense physically because the conversion of cloud water to rain (via C_0) is tied strongly to liquid water variables and thus the surface rain rate and accumulation; however, lateral mixing affects the condensation process through the entrainment of dry air, which in turn modifies the TLWC (mostly the cloud water). Note that the percentage changes in each DV show an identical rate of change for α and R, but opposite in sign because the lateral eddy exchange term is proportional to α/R.

Figure 4 shows the sensitivities of rainwater mixing ratio to both C_0 and α. In the control run, strong gradients are evidenced around the AMQ_r (see Fig. 1d). Because an increase in C_0 (Fig. 4a) shortens the life of

TABLE 1. Dimensionless relative sensitivity coefficients (RSC) of dependent variables J_k = (TLWC, SSR, ARF) with respect to physical parameters X_j = (C_0, α, R). The RSC is computed as $(\partial J_k/\partial X_j)(J_k/X_j)^{-1}$.

Parameters (X_j)	$\left(\frac{\partial \text{TLWC}}{\partial X_j}\right)\left(\frac{\text{TLWC}}{X_j}\right)^{-1}$	$\left(\frac{\partial \text{SRR}}{\partial X_j}\right)\left(\frac{\text{SRR}}{X_j}\right)^{-1}$	$\left(\frac{\partial \text{ARF}}{\partial X_j}\right)\left(\frac{\text{ARF}}{X_j}\right)^{-1}$
C_0	−0.0768	1.1273	0.9993
α	−0.2278	−0.0942	−0.0684
R	0.2278	0.0942	0.0684

the cloud, rain forms sooner and terminates earlier than in the control run so that the AMQ_r is shifted to the left along the time axis. The sensitivity fields represent this behavior quite well. Note also that, during the mature stage, the region of negative sensitivity near cloud top occurs just above the region of positive sensitivity, implying that with an increase in C_0, rain is produced at a much faster rate and falls out earlier from the upper portion of the cloud (see Ogura and Takahashi 1971).

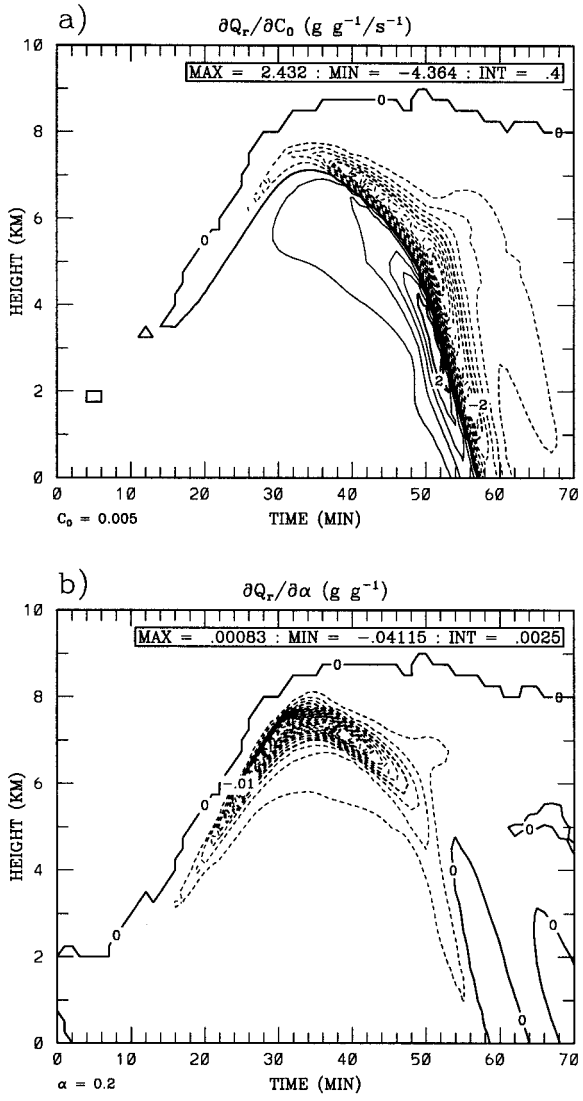

FIG. 4. Sensitivities of Q_r with respect to (a) C_0 (in g g^{-1}/s^{-1}) and (b) α (in g g^{-1}).

An increase in α (Fig. 4b) results in a decrease in Q_r, mostly near cloud top in the region of strong gradients in Q_r (see Fig. 1d). In our model, entrainment occurs via two separate processes (see Ogura and Takahashi 1971 and the appendix of PD97): so-called dynamic entrainment, which is based on mass continuity considerations and proportional to $-\partial(\rho w)/\partial z$, and lateral eddy exchange, which is proportional to $-|w|\alpha/R$. Although the effect of dynamic entrainment might be greater, the sensitivity results presented here are only for lateral eddy exchange via α. As indicated by PD97, an increase in α leads to smaller maximum updraft, lower cloud top, and longer lifetime of the storm though the changes are not significant. During the mature stage, a weaker updraft produces less condensation and thus less conversion of cloud to rain (i.e., negative sensitivity), while a slight change in the cloud depth makes large sensitivities occur in the region of strong gradient near cloud top. During the decaying stage, the sensitivity fields tilt downward with time similarly to the AMQ_r, which results from a time shift of the AMQ_r due to the longer lifetime of the storm.

b. Sensitivity to environmental characteristics

Until now, we have focused on changes in storm behavior induced by variations in specific parameters of the model. We now turn to the environment and compute sensitivity fields for changes in selected environmental properties. The DV is chosen to be the TLWC, and the IVs are the (stationary) environmental temperature (T_{env}) and water vapor mixing ratio ($Q_{v\text{env}}$) at all grid points. The sensitivities of TLWC are computed at t = 25, 45, and 57 min, corresponding to the updraft maximum, the late mature stage of the storm, and the maxima in downdraft and SRR, respectively (see Figs. 1 and 2).

The change in TLWC throughout the entire storm's life is most strongly affected by changes at low levels in both T_{env} and $Q_{v\text{env}}$. As shown in Fig. 5a, the TLWC decreases due to an increase in T_{env} at middle and low levels, except at the ground where it increases rather markedly. An increase in T_{env} affects the thermal buoyancy in two ways. First, it acts directly in the vertical momentum equation to decrease the buoyancy, which results in a weaker updraft and a lower rate of liquid

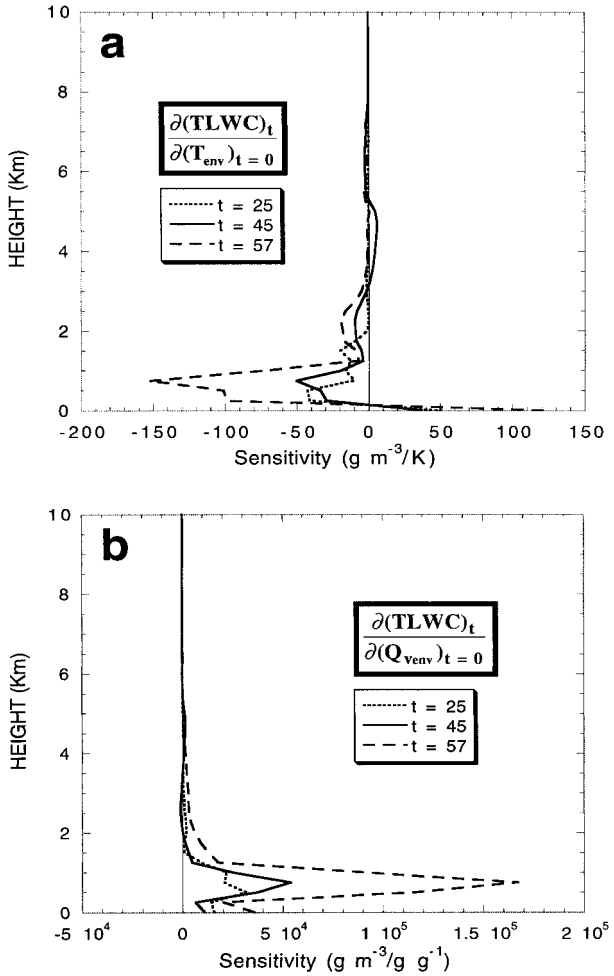

FIG. 5. Sensitivities of TLWC at $t = 25$, 45, 57 min with respect to (a) T_{env} (in g m^{-3}/K) and (b) Q_{venv} (in g m^{-3}/g g^{-1}) at initial time.

water production. Second, it reduces the amount of cooling through lateral mixing and dynamical entrainment in the thermodynamic energy equation, thereby increasing the buoyancy. While these two effects compete against one other in various locations, our results show that the former affects the TLWC most strongly. It should be kept in mind that these findings are valid only for the particular manner in which our cloud is initialized. Storms initiated via continuous surface heating or topography may show much different sensitivity.

Figure 5b shows that as Q_{venv} increases, especially in the layer below 2 km, the TLWC increases because drying via lateral mixing and dynamical entrainment is reduced. Thus, the amount of evaporation is reduced and the cloud can hold more liquid water.

For both T_{env} and Q_{venv}, the magnitudes of the TLWC sensitivities increase with time. Throughout the entire cloud life cycle, the height at which the largest sensitivities occur (i.e., at $z = 0.5$ km at $t = 25$ min and at $z = 0.75$ km at $t = 45$ and 57 min) is the same for both variables. As explained above, the change in TLWC below 2 km is opposite for the two variables. That is, an increase in the environmental temperature (moisture) results in a decrease (increase) in the TLWC.

Although these results are straightforward and could have been anticipated and computed using other approaches, they do serve to illustrate the power of the analysis procedure described in section 2. In the sections that follow, we apply the technique to investigate aspects of the problem that would be difficult to analyze by other methods.

c. Sensitivity to selected forecast aspects

We now investigate the sensitivity of a few derived (from basic model-predicted fields) DVs to selected forecast aspects both at the initial and later times. The purpose for doing the latter is manifold. First, if one confines the sensitivity analysis to the initial conditions, then the rather artificial manner in which the cloud is initialized in our experiments (i.e., by an impulse in the vertical motion field) becomes the focus and all sensitivity results relate back to that particular and arguably questionable strategy. Second, in the context of actual cloud-scale prediction, numerical models will often be initialized from radar and other observing systems that provide information only after a storm has formed and is perhaps quite mature. Thus, it is important to understand how the model would react to changes in various fields (either observed directly or retrieved) at various locations in both the storm and its environment. Finally, in the context of 4D data assimilation (see section 5), one considers a period of time during which the storm evolves, even though the emphasis is typically on the initial condition as the principal control variable. As a result, it is important to understand how errors inserted with new data during the assimilation process might affect the evolution of the dynamical system.

We also assess in this section the relative importance of initial conditions to the change in DVs via relative sensitivity analysis. Note that our analysis encompasses both domain-wide or integrated (TLWC, ARF) as well as instantaneous (SRR) measures of storm behavior in an effort to characterize overall sensitivity. We believe that an examination of both is necessary to capture the finescale details of cloud sensitivity that are of interest to cloud modelers, as well as the sensitivity of more global properties that are relevant, for example, in cumulus parameterizations.

Figure 6a shows the sensitivity of the SRR to the *initial* Q_v field at the same times noted above ($t = 25$, 45, and 57 min), while Fig. 6b shows the sensitivity to Q_v at $t = 5$, 25, and 45 min of the SRR at a *particular time* ($t = 57$ min). By looking at these contrasting measures of sensitivity, one is able to better evaluate the overall sensitivity in contrast to that with respect only to variables specified at the initial time.

Over the lifetime of the storm, the SRR is influenced almost exclusively by changes in the initial Q_v field

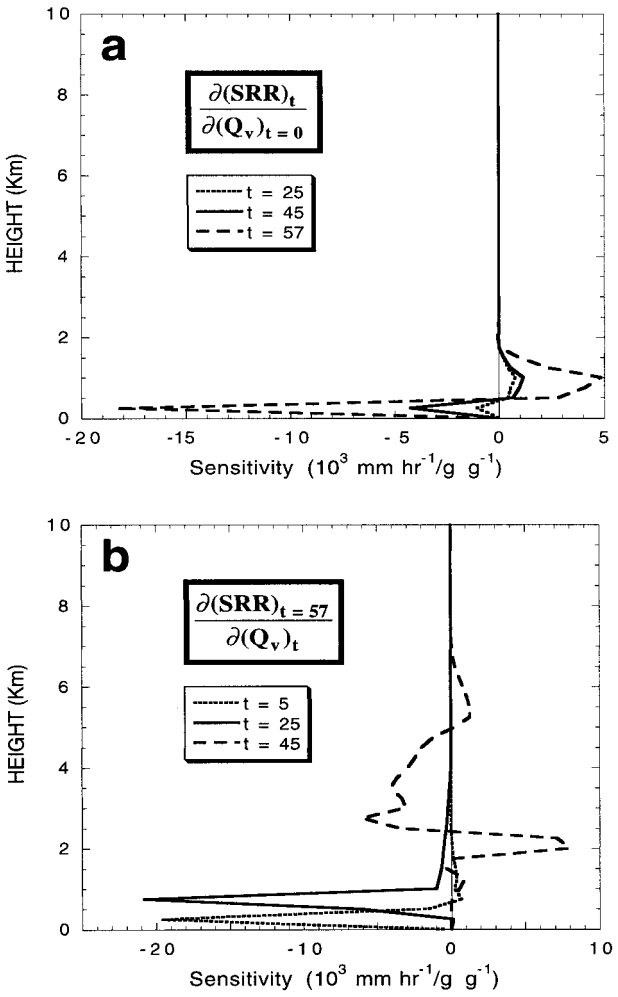

FIG. 6. (a) Sensitivities of SRR at $t = 25$, 45, 57 min with respect to initial Q_v and (b) sensitivities of SRR at $t = 57$ min with respect to Q_v at $t = 5$, 25, 45 min (in 10^3 mm h^{-1}/g g^{-1}).

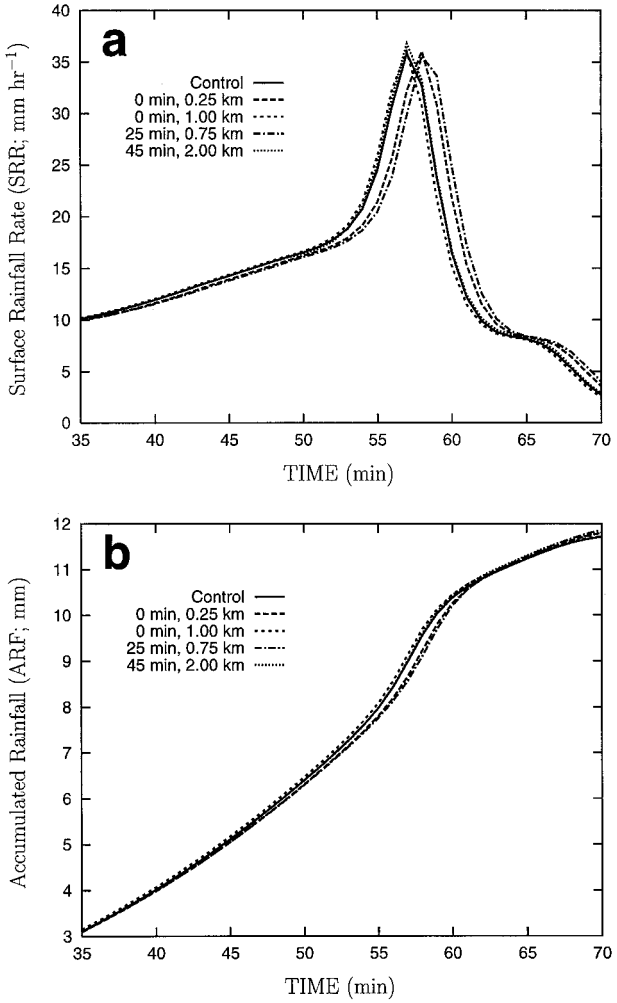

FIG. 7. Nonlinear model results of (a) SRR (in mm h^{-1}) and (b) ARF (in mm) for perturbations of Q_v at various locations and times.

below 2 km (Fig. 6a), as one might expect. The sensitivities are positive from 0.5 to 2 km (peaking at 1 km) and negative below (peaking at 0.25 km). The magnitude of the sensitivity increases with time in both regions. The vertical structure of the sensitivity fields can be explained as follows.

At the lowest model grid point the updraft is initially quite weak and is quickly replaced by downdraft around 5 min (see Fig. 1). Thus, the increased Q_v at $z = 0.25$ km has little opportunity to impact the growing updraft a few kilometers above. Instead, it simply increases the virtual temperature near the ground. This virtual warming induces positive virtual thermal buoyancy (Srivastava 1985, 1987), which delays rainwater sedimentation. Thus, the maximum SRR occurs later and the storm's lifetime extends longer (see Fig. 7a). The fact that the sensitivity becomes stronger with time is consistent with this argument, and with the temporal shifts in evolution that accompany a less or more vigorous cloud.

In contrast, the positive sensitivity exhibited in the region between 0.5 and 2 km shows a maximum at 1 km, which is the height of the maximum vertical velocity specified in the initial conditions. Consequently, an increase in water vapor in this region induces stronger convection creating a more vigorous cloud, greater rates of rain production, and thus greater SRRs. This implies an earlier occurrence of the maximum SRR and shorter lifetime of the storm.

In Fig. 6b, the change in SRR at 57 min is shown for a unit increase in Q_v at selected earlier times. Again, keep in mind that the SRR reaches its maximum at 57 min in the control case. It is interesting that the altitude of the strongest SRR sensitivity to Q_v increases as the time of perturbation approaches 57 min. This behavior is related to the rise of cloud base with time. In fact, the perturbation that results in the largest SRR at 57 min is that located just above cloud base (in the region of weak updraft) at each time shown.

For increases in Q_v during the growing and early

mature stage (e.g., 5 min and 25 min, respectively) near cloud base, the SRR at 57 min shows a marked decrease and the spatial patterns of sensitivities are quite simple. During these stages, the cloud-induced temperature and moisture perturbations near cloud base are quite large. Young (1993) showed that an increase of Q_v in weakly rising warm air can bring about an increase in condensation and provide higher liquid water contents. Note that, in our model, the condensed water is simply converted to rainwater in ~3.3 min. Increased latent heat release due to increased condensation rates can result in an increase in updraft intensity, which reduces the effect of liquid water drag and thus delays rainwater sedimentation. Therefore, the maximum SRR occurs later than the control case. However, this may not necessarily imply weaker cloud development because the increased updraft intensity maintains a greater mass of rain in the cloud, thereby allowing for continued growth by coalescence (Goody 1995).

It is interesting to note that the SRR at 57 min shows little sensitivity to water vapor perturbations at 25 min in either the subcloud layer or at upper levels. At t = 25 min, the subcloud layer is occupied by downdraft. Although condensation may occur in the downdraft region under some circumstances (e.g., Young 1993), the associated latent heat release may decelerate the downdraft and suppress convection. Thus, the amount of condensate tends to be small and the SRR virtually unaffected. At upper levels, the updraft is very strong at t = 25 min. Because the temperature and moisture content in this region are relatively low, the rate of condensation is likewise small. Even though some cloud water is present due to condensation and advection, it is carried rapidly to cloud top and has little opportunity to produce rain. Thus, changes in Q_v at these levels have virtually no impact on the SRR.

To verify our interpretation on the behavior of the sensitivities, we have run the nonlinear model for an increase of Q_v by 0.1 g kg^{-1} at various locations and times. The SRR and ARF fields for these perturbation runs are shown in Fig. 7. Note that the same amount of perturbation is given to all cases. It is apparent that the water vapor perturbations bring about time shifts in both SRR and ARF for most cases. However, when Q_v is increased at 2 km at 45 min, the SRR shows a decrease for a short period then an increase throughout the simulation time (cf. with Fig. 6b). This can be explained as the following. Note that the perturbation is added to a weak updraft region that is being replaced by downdraft in a few minutes. An increase in Q_v in that region induces an increase in updraft as well as in liquid water as explained above thus delays falling of raindrops. But the updraft yields to the strong downdraft that occupies the region rapidly. This downdraft accelerates falling of the suspended raindrops afterward. Although the ARF fields show quite big differences around 57 min, especially for the Q_v perturbations added at 0.25 km at initial time and 0.75 km at 25 min, they end up with similar values for all perturbation cases. This again assures that the strong negative sensitivities in SRR for the two cases (see Fig. 6) are mainly due to the time shifts.

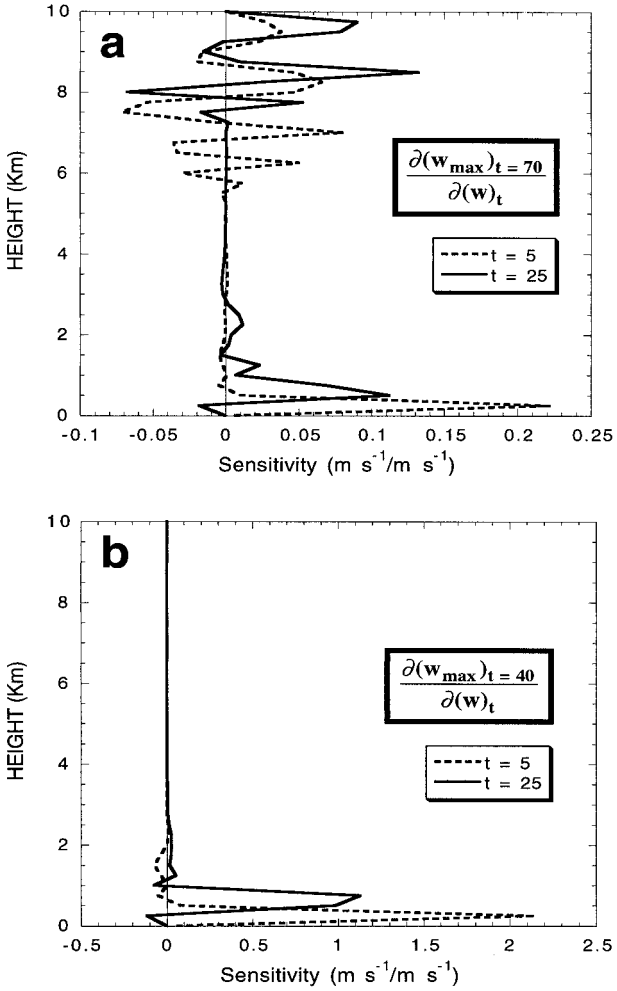

FIG. 8. Sensitivities of w_{max} at (a) t = 70 min and (b) t = 40 min with respect to w at t = 5 and 25 min (in m s^{-1}/m s^{-1}); w_{max} at 70 min is less than 1 m s^{-1} (at ~8 km) while w_{max} at 40 min is 8 m s^{-1} (at ~5.5 km).

We show in Fig. 8a vertical profiles of the sensitivity of maximum updraft (w_{max}) at 70 min to the w field at earlier times. (Note that w_{max} at 70 min is $<$1 m s^{-1} at an altitude of about 8 km.) Immediately evident is the fact that w_{max} at 70 min is influenced by changes in w from two distinct regions: the lower and upper troposphere. Larger vertical velocities at low levels lead to increases of w_{max} at 70 min. As one might expect, the influence of low-level vertical velocity perturbations on subsequent cloud behavior is greatest at earlier times and lower altitudes. At upper levels, the sensitivity shows a complex pattern with no preference for positive or negative values.

We attribute this structure to the fact that w_{max} at 70 min is located in the region of oscillations near cloud

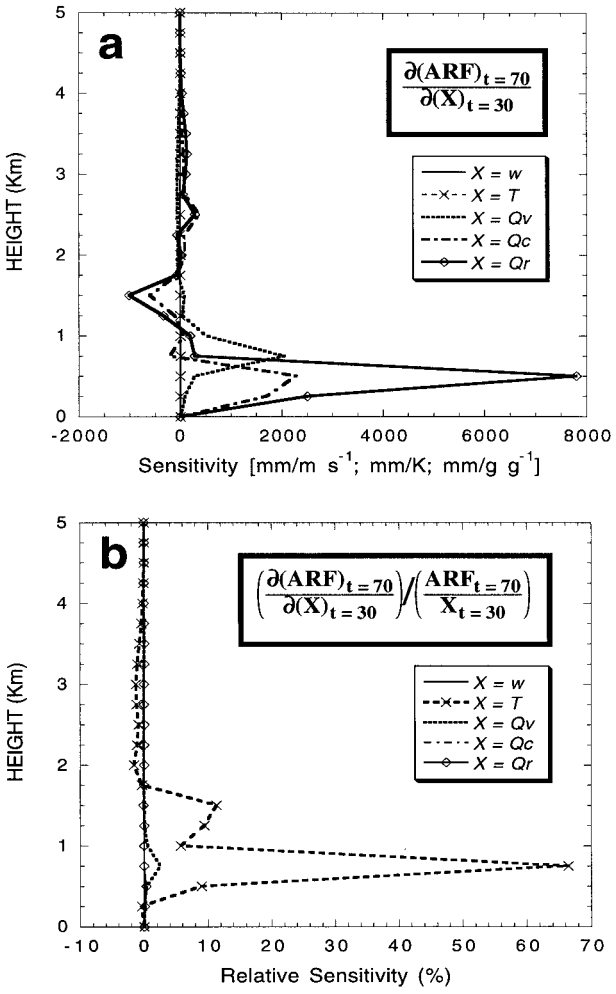

FIG. 9. (a) Standard and (b) relative sensitivities of ARF with respect to w, T, Q_v, Q_c, and Q_r at $t = 30$ min. For (a), units are mm/m s^{-1} for w, mm/K for T, and mm/g g^{-1} for Q_v, Q_c, and Q_r.

top, and to validate this hypothesis, we show in Fig. 8b the same sensitivity information, though at $t = 40$ min when the maximum updraft is located well below the region of oscillations ($w_{max} = 8$ m s^{-1} at about 5.5 km above the ground). Note that the sensitivity drops off rapidly with height above the boundary layer.

We now consider the *relative* importance of various fields on cloud evolution using the procedure described earlier. Figure 9 shows both the regular and relative sensitivity coefficients of the final ($t = 70$ min) ARF to all model variables at $t = 30$ min, which is 5 min after the occurrence of maximum updraft (see Figs. 1a and 2a).

Focusing first on Fig. 9a, the sensitivity of ARF with respect to w and T would appear to be negligible compared to that for the moisture variables. The ARF exhibits a significant response only for changes in Q_v in the lowest 1.25 km of the model atmosphere, and for changes in Q_c and Q_r in the lowest 4 km in both cases as one would expect. Note that, at 30 min, cloud base is located at ~0.75 km (see Fig. 1c), and it is at this altitude where the sensitivity of ARF to Q_v is greatest. The response of the ARF to unit increases in Q_c and Q_r are qualitatively similar, though with maxima at different altitudes.

The potentially misleading nature of the above results is revealed in the *relative* sensitivity fields (Fig. 9b), which show that changes in T (at 30 min) have the largest impact on the ARF. The second largest sensitivity is caused by Q_v, but with a much smaller magnitude. The percentage changes in ARF due to a 1% change in other fields (w, Q_c, and Q_r) are almost negligible. Spatially, the largest impact on ARF is produced by the T field near cloud base (~0.75 km), with a local maximum at 1.5 km. Indeed, at 0.75 km, a 1% increase in T yields a ~68% increase in ARF while that in Q_v affords a ~2% increase. A qualitatively similar result is obtained in Park and Droegemeier (1995) for a different dependent variable (a square distance between the perturbation and control run) and for a different time ($t = 0$ min). This analysis underscores the highly nonlinear behavior of deep convection, and demonstrates that a small perturbation in temperature can have a dramatic impact on subsequent cloud evolution. *In so doing, it also suggests the necessity of accurate temperature measurements or retrievals, especially near cloud base and in the lower part of the cloud, for storm-scale modeling and prediction.*

d. Interaction between the wind and thermodynamic fields

Linkages between the wind and thermodynamic fields, especially with regard to dynamical balance, have long been an important issue in numerical weather prediction (e.g., Haltiner and Williams 1980; Warner and Keyser 1984). On the meso- and synoptic scales, the wind errors maintain their original magnitude during the forecast whereas the thermodynamic field errors are dispersed via inertial–gravity waves, as would be expected from classical geostrophic adjustment theory (Blumen 1972). On the storm scale, in which the flow is dominated by advection and moist convective dynamics, the way in which initial errors are manifest between the wind and thermodynamic fields will likely be quite different. One can obtain information on this issue through a sensitivity analysis.

1) SENSITIVITY OF THE WIND FIELD TO THE THERMODYNAMIC FIELD

Figure 10 shows the sensitivity field of w at 55 min to T at 35 and 50 min. The labels on each axis show the height for the variables of interest. When the T field (independent variable; abscissa) is perturbed at 35 min in the lowest 1 km, it evokes a response in w (dependent variable; ordinate) at 55 min throughout the entire layer below cloud top (Fig. 10a). The sensitivity is divided

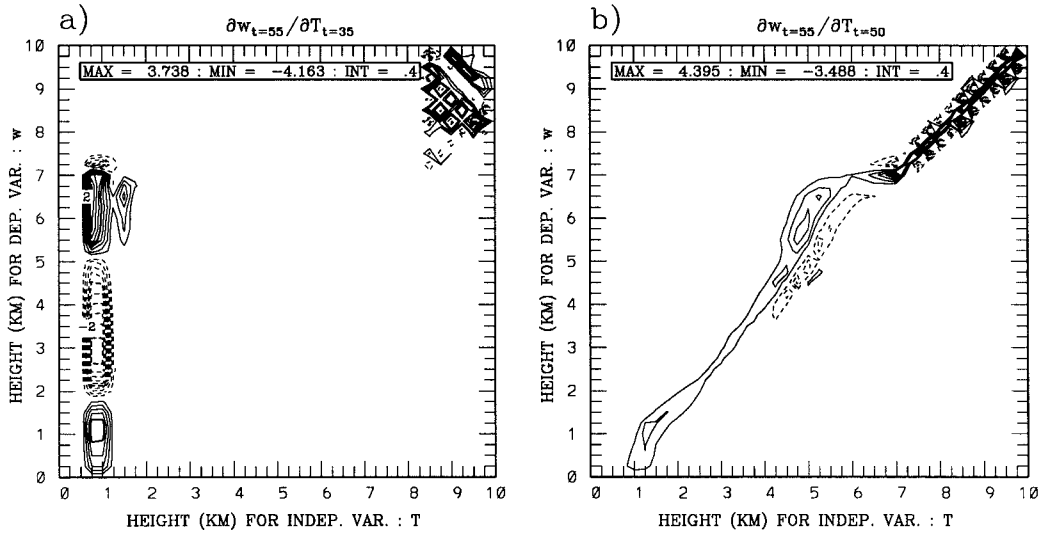

FIG. 10. Sensitivities of w at all levels at $t = 55$ min with respect to T at all levels at (a) $t = 35$ min and (b) $t = 50$ min (in m s^{-1}/°C).

into three regions: positive in both the lower and upper levels and negative in the middle levels. The greatest sensitivity occurs for changes in T near 1 km (cloud-base height at 35 min), with a positive sign (i.e., an increase in T in this region leads to an increase in w by the amount shown on the contour multiplied by the change specified in T). A similar behavior was observed for sensitivities at earlier times, though at lower altitudes. A prominent oscillation in the w sensitivity at upper levels above cloud top is observed for the change in T at the same location (upper-right corner), which is strongly related to the gravity waves.

According to these results, the updrafts between 5 and 7 km at 55 min (see Fig. 10a) increase for positive temperature perturbations at low levels at 35 min. Although the downdrafts increase between 1.75 and 5 km and decrease below 1.75 km due to the same increase in temperature, this behavior is related to the extension of storm lifetime. Note that the local maxima in downdraft intensity occur earlier than 55 min, between 1.75 and 5 km, while they occur later in the layer below 1.75 km (see Fig. 1a). The negative sensitivities in the middle levels and the positive sensitivities in the lower and upper levels are consistent with a shift of the w field to the right along the time axis, which is associated with a longer-lived storm. The nonlinear perturbation run showed an extension of cloud lifetime by 3 min due to a 1°C increase in T at 1 km and 35 min (not shown).

It is interesting that the vertical velocity at 55 min (all levels) shows very weak (below the contour increment, but also nonzero) sensitivity to T at 35 min in the region between 2 to 8 km, that is, above cloud base. While we cannot offer a definitive explanation, recall that the vertical velocity field is most strongly affected by the temperature field *relative* to other variables. Consequently, a given change of temperature will have a smaller relative impact on the buoyancy when temperature excesses are large (i.e., above cloud base) and, thus, a smaller impact on the vertical velocity field.

The sensitivity fields show considerably different structure when perturbations are introduced at later times. As an example, Fig. 10b shows that the response in the vertical velocity field is local to the region for which temperature is perturbed (i.e., along the diagonal line of equal heights for the dependent and independent variables). Note, however, that this effect becomes *less* pronounced as the time between the insertion of the perturbation and the measurement of the response increases.

2) SENSITIVITY OF THE THERMODYNAMIC FIELD TO THE WIND FIELD

We now repeat the analysis of the previous section to examine the dynamical response of the thermodynamic field to changes in the wind field. (Note that we do not discuss relative sensitivity here and are not comparing the relative importance between two fields.) Figure 11a shows the sensitivity of T at 55 min to w at earlier times. The cloud temperatures are impacted primarily by perturbations in w below 1.5 km (Fig. 11a), showing a negative response from 0.5 to 2.5 km (i.e., below cloud base, which is at ~3 km) and a positive response from there up to about 8 km. In the control run (Fig. 1b), a local minimum in T occurs a few minutes prior to 55 min between 0.5 and 2.75 km. Thus, the sensitivity result also reflects the extension of cloud lifetime due to an increase in w at low levels at 35 min.

At later times (Fig. 11b), the sensitivity pattern has features similar to those in Fig. 10b (i.e., tilting but with a broader band structure). Thus, the region of w having the greatest influence on T occurs at higher levels as time increases for the reason noted earlier.

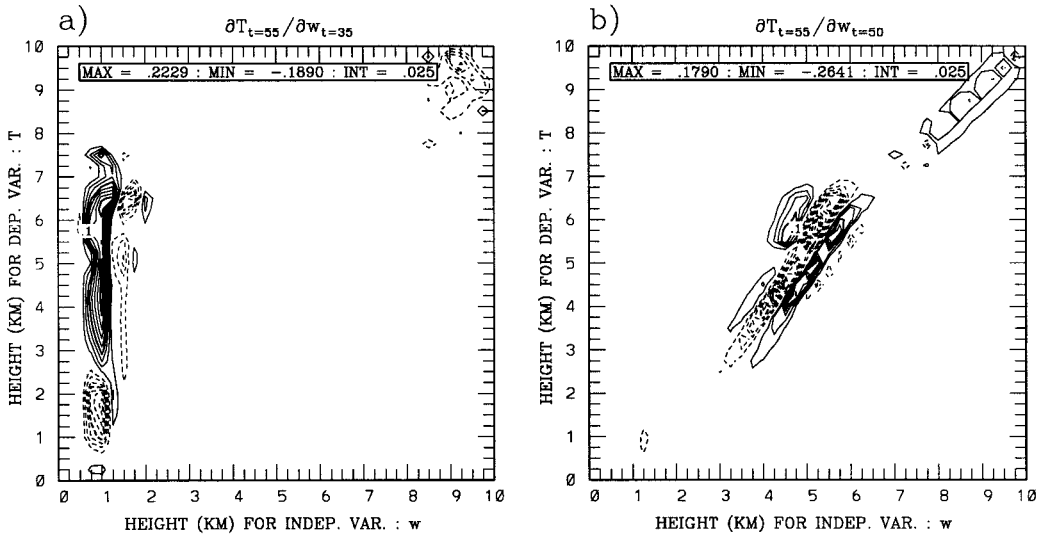

FIG. 11. Same as in Fig. 10 except for sensitivities of T with respect to w (in °C/m s^{-1}).

e. *Sensitivity of rainwater to the wind and thermodynamic fields*

We now examine how errors in the wind and thermodynamic fields influence the rainwater by computing the sensitivity of Q_r with respect to both w and T, the former of which is shown in Fig. 12. During the early stages of storm development, the largest sensitivity in Q_r is observed near cloud top for changes in initial w below 1.5 km (not shown). Similar features are observed in the sensitivity fields at later times (Fig. 12). Note that the boundary of the sign change in the Q_r sensitivity fields occurs at lower levels with time (cf. Figs. 12a and 12b). It is apparently related to the downward tilting of the AMQ_r during the late mature and the decaying stages, and the boundary is coincident with the occurrence of AMQ_r (see Fig. 1d). For an increase in the initial w at 0.25 km, the Q_r sensitivities at both times are positive above the boundary and negative below it. This implies that the occurrence of AMQ_r is delayed; hence, an extension of the cloud's lifetime. For an increase in initial w in the layer 0.5–1.5 km, the Q_r fields change in the opposite direction, implying a shorter lifetime for the perturbed storm, due perhaps in part to increased entrainment above the boundary layer.

We compare in Fig. 13 the sensitivity of Q_r at t = 55 min to w and T at t = 50 min, that is, during the time when banded structures are present in the sensitivity fields. The Q_r sensitivities for changes in w appear

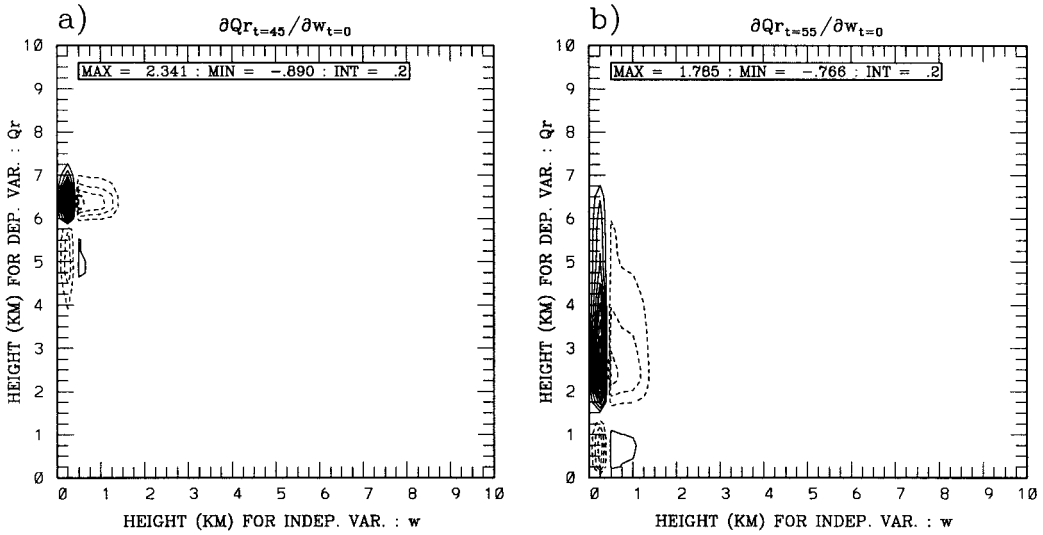

FIG. 12. Sensitivites of Q_r at all levels at (a) t = 45 min and (b) t = 55 min with respect to the initial w field at all levels (in 10^{-3} g g^{-1}/m s^{-1}).

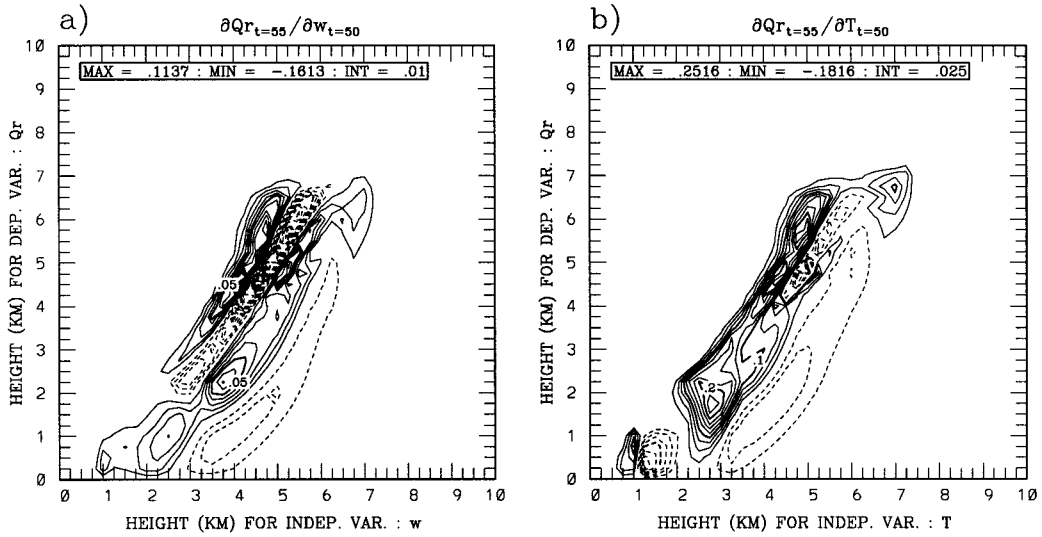

FIG. 13. Sensitivites of Q_r at all levels at $t = 55$ min with respect to (a) w (in 10^{-3} g g^{-1}/m s^{-1}) and (b) T (in 10^{-3} g g^{-1}/°C) at all levels at $t = 50$ min.

in two bands below 2 km, four bands between 2 and 5.5 km, and three bands between 5.5 and 7 km (Fig. 13a). It is notable that, compared to the T sensitivities (see Fig. 11b), the Q_r field exhibits non-negligible changes below 2 km for the same amount of change in initial w between 0.75 and 5.5 km. The sensitivity of Q_r with respect to T exhibits four bands below 1 km, two bands between 1 and 4 km, four bands between 4 and ~6 km, and three bands between ~6 and 7 km (Fig. 13b). Compared to the sensitivities of the thermodynamic and wind fields, the sensitivity of Q_r at a specific level is affected by a broader area of IVs, that is, the bandwidth is much larger (cf. Fig. 13a to Fig. 11b and Fig. 13b to Fig. 10b).

We note that the greatest response in Q_r occurs when perturbations are added at lower levels (below ~1 km) in initial w. This is due partly to the higher lapse rate below 1 km (8.6°C km^{-1}) than above (6.3°C km^{-1}). With a positive perturbation in initial w below 1 km, compared to the case with the same perturbation above 1 km, the air experiences less adiabatic cooling and thus a smaller temperature deficit. This reduces the negative thermal buoyancy, yielding a relatively more favorable condition for storm development. This behavior is also related to the initial w profile and associated differences in dynamical entrainment around 1 km. In our model, dynamical entrainment becomes zero when $\partial \rho w/\partial z < 0$, which occurs above 1 km at the initial time. Thus, perturbations in w below 1 km produce more significant contributions to storm evolution than those above.

It is interesting, and in fact disturbing, to note that small changes in the location of the IV perturbation can lead to radically different outcomes in the DV, particularly as a function of storm maturity, even in this simple 1D model. As an example, Fig. 14 shows the true nonlinear sensitivity of Q_r for a 1% perturbation in initial w at $z = 0.25$ (Fig. 14a) and 0.5 km (Fig. 14b). These may be compared with their linear sensitivity counterparts in Fig. 12 at various times. The initial perturbations in w at both locations in Fig. 14 change the Q_r fields in the same (positive) direction during the growing stage; however, after $t = 34$ min, where the maximum in TLWC occurs and the cloud top reaches its maximum height, the changes in Q_r are of opposite sign and similar magnitude. This suggests that errors below the level of measurement or retrieval uncertainty can alter significantly the evolution of a storm. It is worth noting that the magnitude, sign, and location of the sign change at all times in the nonlinear sensitivity results match perfectly those of the linear sensitivity (see Fig. 12), thus verifying the correctness of our calculations.

5. Summary and conclusions

Using a time-dependent 1D warm-rain cloud model, we investigated the sensitivity of various model outputs to initial and intermediate model states and physical parameters using a deterministic approach for an isolated deep convective cloud. An automatic differentiation tool, ADIFOR, was used to compute sensitivities of all dependent variables (DVs) with respect to all independent variables (IVs). A subset of these sensitivities was discussed with reasonable physical explanations. These linear sensitivities were shown to be adequate for describing the true nonlinear sensitivity provided that the amplitude of the perturbations was sufficiently ''small'' (see Park and Droegemeier 1997).

Among physical parameters, we investigated the effects on storm dynamics of the cloud-to-rain autoconversion factor (C_0), the lateral mixing coefficient (α), and the cloud radius (R). The impact of C_0 was manifest

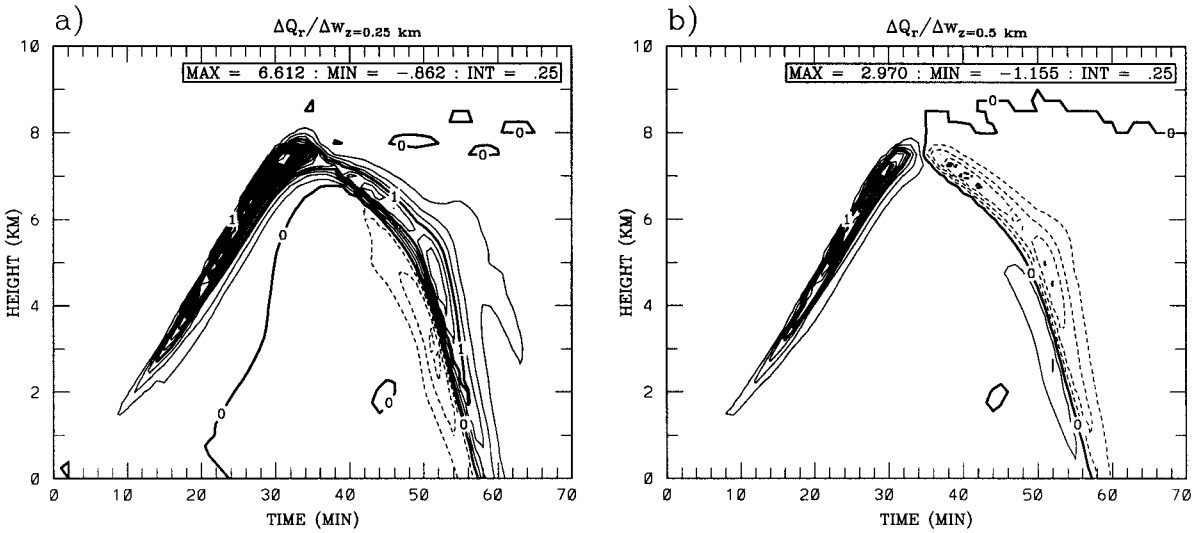

FIG. 14. Nonlinear sensitivities of Q_r for 1% perturbations in w at initial time at (a) $z = 0.25$ km and (b) $z = 0.5$ km (in 10^{-3} g g^{-1}/m s^{-1}).

primarily as an extension in storm lifetime. As C_0 increased, rain was produced more quickly and the cloud decayed earlier due to associated evaporation and liquid water drag. Because both α and R appear in the lateral mixing terms, which also contain the vertical velocity (w), changes in the former were strongly related to the latter. More specifically, mixing of dry air through the lateral boundary of the cloud resulted in less condensation and thus smaller total liquid water content (TLWC). However, increasing the radius of cloud reduced the effect of dry air mixing (in the absence of pressure forces).

We also investigated the sensitivity of storm development to changes in environmental temperature and moisture fields, and found that they produced opposing effects on the TLWC sensitivity. As the environmental temperature increased, the thermal buoyancy became weaker, which resulted in a weaker updraft and a slower rate of liquid water production. As the environmental moisture increased, mixing due to entrainment became weaker; hence, the cloudy air exhibited less evaporation and contained more liquid water. Consequently, an increase in the environmental temperature (moisture) resulted in a decrease (increase) in TLWC.

Sensitivity coefficients were also computed for some diagnostic dependent variables with respect to selected forecast variables. We first examined the sensitivity of surface rainfall rate (SRR) to the water vapor mixing ratio (Q_v). The SRR was found to be sensitive to changes in initial Q_v below 2 km; however, perturbations in different locations and times led to different behavior at later times. For example, Q_v perturbations added near cloud base during the growing and early mature stages of the storm brought about a stronger updraft as well as larger liquid water contents. The associated greater suspension of water aloft led to a delay in storm collapse, that is, a decrease in SRR prior to the time at which the maximum SRR occurred in the control run and an increase thereafter. This same mechanism operated when an identical perturbation was added near cloud base during the late mature stage, except that the updraft region was rapidly occupied by strong downdraft, thus increasing the SRR throughout the rest of the simulation.

For a period when the convective updrafts were most intense, the accumulated surface rainfall (ARF) was found to be most sensitive, in an absolute sense, to changes in rainwater, followed by cloud water and water vapor. It showed virtually no sensitivity to the temperature and vertical motion fields. In sharp contrast, when one examines the relative importance of these variables in controlling the ARF, the temperature produces the greatest impact and its effects are maximized for perturbations inserted at low levels. This relative sensitivity analysis suggests the need for highly accurate temperature measurement or retrievals in the lower part of the cloud.

We also examined the relationship between the thermodynamic and wind fields. For perturbations introduced early in the evolution of the storm, most of the variability in model-predicted fields was confined to the region near cloud top during the growing and early mature stages. It then spread downward with time. When perturbations were inserted during the late mature stage, the response in the DVs was largely confined to the perturbed region. Perturbations in the thermodynamic field above cloud top induced prominent oscillations in the wind field, whereas the reverse was not true. Increases in both fields at low levels resulted in an extension of storm lifetime.

The rainwater (Q_r) field responded in a qualitatively similar fashion to perturbations in both the wind and thermodynamic fields at the initial time. The greatest response in Q_r occurred when perturbations in w were

added below ~1 km. This is partly related to the higher lapse rate below 1 km, resulting in less negative buoyancy and thus more favorable conditions for strong convection. It is also related to the initial *w* profile and the related changes in dynamical entrainment around 1 km at the initial time. The area of sensitivity for the rainwater field was found to be much larger than for the wind and temperature. In other words, perturbations that led to significant changes in the wind and temperature fields were typically confined to a much smaller area of the domain compared to those resulting in marked changes in the precipitation field.

Overall, we found that storm dynamics were controlled principally by changes in initial model states below 2 km, as one might expect. After the initial time, the largest changes in storm behavior occurred at higher levels as perturbations were introduced later in the simulations. Because storm dynamics respond differently to perturbations in different locations, each grid variable in the model, once perturbed, plays its own unique role in determining the dynamical evolution of the storm. In the context of numerical prediction, our results suggest that, in order to predict storm behavior during the decaying stage, one needs accurate observed (or retrieved) fields (especially temperature and moisture) in the subcloud layer during the growing stage and in the entire cloud layer during the late mature and earlier decaying stages. Put another way, the region of influence of the inserted errors increases as the cloud matures.

Although the type of global sensitivity analysis presented here can be extremely expensive as the matrix resulting from the successive multiplication of sparse matrices in ADIFOR becomes dense, it is nonetheless more efficient than a pure forward accumulation strategy. In addition, ADIFOR is very efficient when the number of both IVs and DVs is very large, as in our case. When the number of IVs exceeds the number of DVs such as data assimilation (where one needs to compute the gradient of one variable, the cost function, with respect to all IVs, the initial guess fields), however, the adjoint model approach would be preferred.

Although ADIFOR bypasses the creation of an adjoint code, it provides more information concerning the gradient vector than does the traditional adjoint approach. We therefore feel that the added computational expense (see Park 1996) more than offsets the time and difficulty required to develop an adjoint code manually. For a large number of IVs, parallel processing can be employed to improve the performance of ADIFOR (Park et al. 1994).

We close by noting that the results obtained here are valid for a very simple 1D cloud model that lacks the physical realism needed to simulate other types of storms that are inherently three-dimensional. Nevertheless, we felt it appropriate to start with a 1D model because it embodies the basic physical processes of more sophisticated models, and because it represented a tractable convective dynamics problem to which ADIFOR could be applied. An analysis similar to that presented here has now been conducted for a 3D supercell storm and is reported in a separate paper (in preparation).

Additional studies are needed to address, in a more general sense, the impact of initial and boundary condition uncertainties in convective-scale dynamics and prediction, particularly with regard to ensemble forecasting and targeted observations. While the results described herein paint a somewhat pessimistic picture of the prospects for convective-scale NWP, we note that important forcing mechanisms (e.g., terrain, fronts, drylines, surface inhomogeneities) that tend to focus and control convective evolution have not been considered here and may counter some of our disturbing results. Experiments including these and other influences are now under way.

Acknowledgments. We are grateful to Dr. Chris Bischof, Mr. Tim Knauff, and Mr. Andrew Mauer at Argonne National Laboratory for their assistance in applying ADIFOR to our model. Additionally, the detailed comments provided by two anonymous reviewers improved significantly the quality of this paper, and to them we extend our gratitude. This research was supported by the National Science Foundation under Grant ATM92-22576 to the second author, and by Grant ATM91-20009 to the Center for Analysis and Prediction of Storms at the University of Oklahoma. The simulations were performed on the Cray C90 at the Pittsburgh Supercomputing Center.

REFERENCES

Bischof, C., A. Carle, G. Corliss, A. Griewank, and P. Hovland, 1992: ADIFOR—Generating derivative codes from Fortran programs. *Sci. Program.,* **1,** 11–29.

——, G. D. Pusch, and R. Knoesel, 1996: Sensitivity analysis of the MM5 weather model using automatic differentiation. *Comput. Phys.,* **10,** 605–612.

Blumen, W., 1972: Geostrophic adjustment. *Rev. Geophys. Space Phys.,* **10,** 485–528.

Cacuci, D. G., 1988: The forward and adjoint methods of sensitivity analysis. *Uncertainty Analysis,* Y. Ronen, Ed., CRC Press, 71–144.

Carmichael, G. R., A. Sandu, and F. A. Potra, 1997: Sensitivity analysis for atmospheric chemistry models via automatic differentiation. *Atmos. Environ.,* **31,** 475–489.

Curic, M., and D. Janc, 1989: Sensitivity analysis of the 1-D convective cloud model outputs on the dynamical parameters. *Theor. Appl. Climatol.,* **40,** 237–246.

——, and ——, 1993: Predictive capabilities of a one-dimensional convective cloud model with forced lifting and a new entrainment formulation. *J. Appl. Meteor.,* **32,** 1733–1740.

Dickinson, R. P., and R. J. Gelinas, 1976: Sensitivity analysis of ordinary differential equation systems—A direct method. *J. Comput. Phys.,* **21,** 123–143.

Errico, R. M., and T. Vukicevic, 1992: Sensitivity analysis using an adjoint of the PSU–NCAR mesoscale model. *Mon. Wea. Rev.,* **120,** 1644–1660.

Ferrier, B. S., and R. A. Houze Jr., 1989: One-dimensional time-dependent modeling of GATE cumulonimbus convection. *J. Atmos. Sci.,* **46,** 330–352.

Goody, R., 1995: *Principles of Atmospheric Physics and Chemistry*. Oxford University Press, 324 pp.

Haltiner, G. J., and R. T. Williams, 1980: *Numerical Prediction and Dynamic Meteorology*. 2d ed. John Wiley and Sons, 477 pp.

Holton, J. R., 1992: *An Introduction to Dynamic Meteorology*. 3d ed. Academic Press, 507 pp.

Hwang, J.-T., E. P. Dougherty, S. Rabitz, and H. Rabitz, 1978: The Green function method of sensitivity analysis in chemical kinetics. *J. Chem. Phys.,* **69,** 5180–5191.

Ogura, Y., and T. Takahashi, 1971: Numerical simulation of the life cycle of a thunderstorm cell. *Mon. Wea. Rev.,* **99,** 895–911.

——, and ——, 1973: The development of warm rain in a cumulus model. *J. Atmos. Sci.,* **30,** 262–277.

Park, S. K., 1996: Sensitivity analysis of deep convective storms. Ph.D. thesis, University of Oklahoma, 245 pp. [Available from School of Meteorology, University of Oklahoma, Norman, OK 73019.]

——, and K. K. Droegemeier, 1995: On the use of automatic differentiation to assess parametric sensitivity in convective-scale variational data assimilation. *Second Int. Symp. on Assimilation of Observations in Meteorology and Oceanography*, Vol. 1, WMO/TD-No. 651, 111–116.

——, and ——, 1997: Validity of the tangent linear approximation in a moist convective cloud model. *Mon. Wea. Rev.*, **125,** 3320–3340.

——, ——, C. Bischof, and T. Knauff, 1994: Sensitivity analysis of numerically-simulated convective storms using direct and adjoint methods. Preprints, *10th Conf. on Numerical Weather Prediction*, Portland, OR, Amer. Meteor. Soc., 457–459.

Seigneur, C., T. W. Tesche, P. M. Roth, and L. E. Reid, 1981: Sensitivity of a complex urban air quality model to input data. *J. Appl. Meteor.*, **20,** 1020–1040.

Soong, S.-T., and Y. Ogura, 1973: A comparison between axisymmetric and slab-symmetric cumulus cloud models. *J. Atmos. Sci.*, **30,** 879–893.

Srivastava, R. C., 1985: A simple model of evaporatively driven downdraft: Application to microburst downdraft. *J. Atmos. Sci.*, **42,** 1004–1023.

——, 1987: A model of intense downdrafts driven by the melting and evaporation of precipitation. *J. Atmos. Sci.,* **44,** 1752–1773.

Sykes, J. F., J. L. Wilson, and R. W. Andrews, 1985: Sensitivity analysis for steady state groundwater flow using adjoint operators. *Water Resour. Res.*, **21,** 359–371.

Wang, J. Y. C., 1983: A quasi-one-dimensional, time-dependent and non-precipitating cumulus cloud model: On the bimodal distribution of cumulus cloud height. *J. Atmos. Sci.,* **40,** 651–664.

Wang, Z., K. K. Droegemeier, M. Xue, and S. K. Park, 1995: Sensitivity analysis of a 3-D compressible storm-scale model to input parameters. *Second Int. Symp. on Assimilation of Observations in Meteorology and Oceanography*, Vol. 1, WMO/TD-No. 651, 437–442.

Warner, T. T., and D. Keyser, 1984: Some practical insights into the relationship between initial state uncertainty and mesoscale predictability. *Predictability of Fluid Motions*, G. Holloway and B. J. West, Ed., American Institute of Physics Conference Proceedings, Vol. 106, 271–286.

Weinstein, A. I., 1970: A numerical model of cumulus dynamics and microphysics. *J. Atmos. Sci.,* **27,** 246–255.

Wisner, C., H. D. Orville, and C. Myers, 1972: A numerical model of a hail-bearing cloud. *J. Atmos. Sci.,* **29,** 1160–1181.

Worley, B. A., E. M. Oblow, F. G. Pin, R. E. Maerker, J. E. Horwedel, R. Q. Wright, and J. L. Lucius, 1987: Deterministic methods for sensitivity and uncertainty analysis in large-scale computer models. *Proceedings of the Conference on Geostatistical, Sensitivity, and Uncertainty Methods for Ground-Water Flow and Radionuclide Transport Modeling*, B. E. Buxton, Ed., Battelle-Press, 135–154.

Young, K. C., 1993: *Microphysical Processes in Clouds.* Oxford University Press, 427 pp.